H-mode discharges with feedback-controlled radiative boundary in the ASDEX Upgrade tokamak

A. Kallenbach et al.

IPP 1/284 Januar 1995

MAX-PLANCK-INSTITUT FÜR PLASMAPHYSIK

85748 GARCHING BEI MÜNCHEN

MAX-PLANCK-INSTITUT FÜR PLASMAPHYSIK

GARCHING BEI MÜNCHEN

H-mode discharges with feedback-controlled radiative boundary in the ASDEX Upgrade tokamak

A. Kallenbach et al.

IPP 1/284 Januar 1995

Die nachstehende Arbeit wurde im Rahmen des Vertrages zwischen dem Max-Planck-Institut für Plasmaphysik und der Europäischen Atomgemeinschaft über die Zusammenarbeit auf dem Gebiete der Plasmaphysik durchgeführt.

H-mode discharges with feedback-controlled radiative boundary in the ASDEX Upgrade tokamak

A. Kallenbach, R. Dux, V. Mertens;
O. Gruber, G. Haas, M. Kaufmann, W. Poschenrieder, F. Ryter, H. Zohm;
M. Alexander, K. Behringer, M. Bessenrodt-Weberpals, H.-S. Bosch, K. Büchl,
A. R. Field, J. C. Fuchs, O. Gehre, A. Herrmann, W. Köppendörfer, K. Lackner, F. Mast,
G. Neu, J. Neuhauser, S. de Peña Hempel, G. Raupp, K. Schönmann, A. Stäbler,
K.-H. Steuer, O. Vollmer, M. Weinlich, W. P. West*, T. Zehetbauer,
and the ASDEX Upgrade Team
Max-Planck-Institut für Plasmaphysik, EURATOM Association,
D–85748 Garching, Federal Republic of Germany
* *General Atomics, San Diego, USA*

January 11, 1995

Abstract

Puffing of impurities (neon, argon) and deuterium gas in the main chamber is used to simultaneously feedback-control the total radiated power fraction and the divertor neutral particle density in the ASDEX Upgrade tokamak. The variation of $P_{sep} = P_{heat}$-P_{rad}(core) by impurity radiation during H-mode shows a similar effect on the ELM behaviour as that obtained by a change of the heating power. For radiated power fractions above 90 %, the ELM amplitude becomes very small and detachment from the divertor plates occurs, whilst no degradation of the global energy confinement is observed (Completlely Detached High-confinement mode). Additional deuterium gas puffing is found to increase the radiated power per impurity ion in the plasma core due to the combined effect of a higher particle recycling rate and a lower core penetration probability. The outer divertor chamber, which is closed for deuterium neutrals, builds up a high neutral pressure the magnitude of which is determined by the balance of particle sources and pumping. For this particular situation, the effective pumping time of neon and argon is considerably accelerated to less than 0.3 s mainly due to

an improved divertor retention capability. The radiation characteristic of discharges with a neon-driven radiative mantle are modelled using a 1-d radial impurity transport code which has been coupled to a simple divertor model describing particle recycling and pumping. The results of simulations are in good agreement with experiment.

1 Introduction

The concept of a radiating boundary is a promising option for the reduction of the power flow onto the target plates required for future reactors. Controlled puffing of medium-Z impurities (e.g. noble gases) leads to enhanced radiative power losses by partially ionized atoms, which have to be restricted to the plasma edge to preserve good global energy confinement. Such 'cold plasma mantle' concepts have been known for several years ([1] and references therein), and the feasibility of this principle was recently demonstrated under L-mode conditions on the limiter-tokamak TEXTOR [2]. However, the compatibility of the radiative boundary with high performance discharge scenarios (H-mode) and its applicability to the experimental parameters of a future reactor have still to be achieved. Further critical issues are the fuel dilution by the injected impurities and impurity accumulation.

We have investigated the properties of single-null divertor discharges with feedforward and feedback controlled impurity (neon, argon) puffing and strong additional heating. Main emphasis is placed on the plasma behaviour with neon, which was found to be better suited than argon for power removal in a reactor plasma with flat (H-mode) density profiles in a recent system study [3]. Initial experiments revealed, that the neutral deuterium gas flux is an important parameter influencing the radiative behaviour. This finding led to the development of an independent feedback system for the divertor neutral flux density, and the reciprocal influence of impurity and deuterium injection is analyzed in detail.

The paper is organized as follows. Section 2 describes the experimental arrangement and the main diagnostics relevant for this study. Section 3 gives an overview of the general behaviour of H-mode discharges with impurity and deuterium puffing. Pumping and recycling of injected noble gases are analyzed in section 4, detailed modelling of the neon emisson is presented and compared to the measurements in section 5. Finally, the impact of impurity injection on the energy confinement and the occurence of complete divertor detachment are discussed in Section 6.

2 Experimental arrangement

ASDEX Upgrade is a midsize tokamak (Major radius R=1.65 m, minor radius a= 0.5 m, typical elongation κ= 1.6, plasma surface S$\approx$ 40 m^2), with a single-null divertor configuration. All plasma-facing components are graphite-covered and the vessel is routinely boronized. Particles

are injected by fast valves in the main chamber, which have been calibrated *in situ* for D_2, He, Ne and Ar. Turbomolecular pumps connected to the outer divertor chamber (see Fig. 1) allow exhaust control of the hydrogen and noble gases particle content of the vessel. The pumping speed for D_2 at low pressure is S_{D_2}= 13 m^3/s, increasing to about 18 m^3/s with the neutral pressure in the divertor.

The discharges described in this paper have a safety factor $q_{95} \approx 4$ with plasma currents of I_p= 0.8 or 1 MA and toroidal fields of B_t = 2 or 2.5 T, respectively. Neutral beam heating (H→D or D→D injection) of 4-7 MW is applied which leads to H-mode operation with type-I ELMs [4], [5] for all experimental conditions except cases with strong additional radiative power loss.

Plasma radiation is measured by five bolometer camera systems with a total of 72 chords situated in two different positions as indicated in Fig. 1. Spatial profiles of the radiation are obtained from a deconvolution of the measured chord intensities by off-line analysis, where restrictions have to be applied to details of divertor and X-point radiation due to the limited spatial resolution in this region. The total main chamber radiation P_{rad}^{main} is reliably derived using a straightforward analysis of 30 line integrals taken throughout the plasma bulk above the X-point. For the feedback control, the total radiated power is also calculated in real time from a subset of 12 selected vertical viewing lines during the discharge.

The electron temperature is measured with a 16-channel Thomson scattering system and ECE measurements for certain radial regions. Electron density profiles are derived from the deconvolution of 6 line integrals obtained by DCN interferometry, cross-checked by Lithium beam measurements at the edge and in the SOL.

Absolute values of midplane line-averaged Z_{eff} are available from bremsstrahlung measurements during neon injection or at lower heating power for most of the discharges. However, during high-power phases without neon injection, the bremsstrahlung measurement was disturbed by infrared emission from hot edges of carbon tiles. For some discharges, Ne^{10+} ion densities could be determined from charge exchange recombination spectroscopy using the NeX (10→9) transition at 388.4 nm [6]. The accuracy of these CXRS density measurements is estimated to be within ± 30 % for hydrogen injection, the major uncertainties originating from the beam attenuation calculations and the CXR rate coefficients. For deuterium injection, the experimental uncertainty is higher owing to the stronger beam attenuation. In addition, the rate coefficients are believed to be less accurate for these low beam particle energies (< 30 keV/amu for deuterium), where excited beam neutrals are expected to contribute to the CXR transition rate.

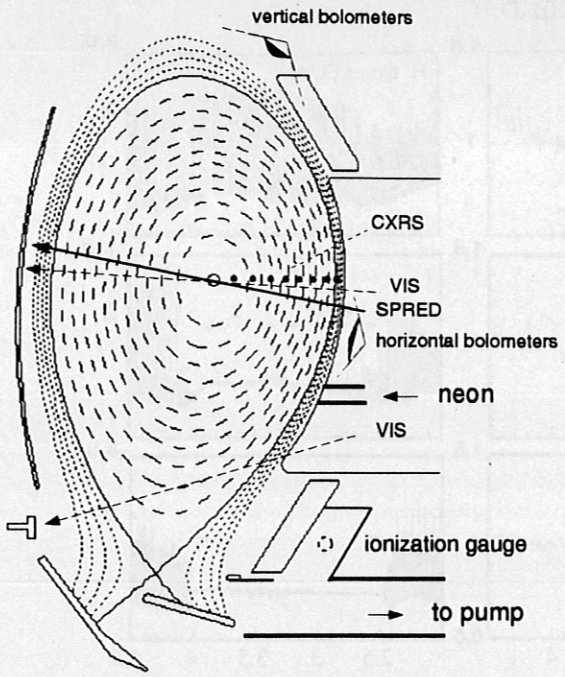

Figure 1: *Plasma cross section with the viewing lines of visible spectroscopy (neon influx) in the midplane and the lower heatshield (HS) region, the SPRED VUV spectrometer and charge exchange recombination spectroscopy (CXRS). In addition, the positions of bolometer cameras and the ionisation gauge for measurement of the neutral divertor flux density are indicated.*

The flux of recycling neutral neon is measured at the midplane and lower inner divertor regions with the absolutely calibrated multichordal spectrometer/camera system otherwise used for CXR spectroscopy [7]. The system consists of a 1-m stigmatic spectrograph with quartz fibers aligned along the entrance slit and an intensified CCD detector providing 11 spatial channels with 50 ms temporal resolution. Neutral neon particle fluxes are estimated from the photon fluxes of the NeI transition at 585.3 nm by multipication with an S/XB value of 15, where the electron impact excitation rate X was taken from [8].

The VUV radiation of various emission lines is measured with the SPRED spectrometer viewing through the plasma midplane with a typical temporal resolution of 20 ms. Calibration of the SPRED system was made via various indirect techniques including branching-ratio measurements and comparison with other diagnostics (CXRS, bolometer, visible spectroscopy). The accuracy of the measured VUV line intensities is estimated to be within a factor of 2.

The neutral flux density $\Gamma_{D_2}^{div}$ in the divertor is measured by fast ionization gauges [9]. Occasionally, the corresponding neutral density $n_{D_2}^{div}$ is used as the more convenient quantity, which is calculated from $\Gamma_{D_2}^{div}$ under the assumption of a thermal Maxwellian neutral distribution at T= 300 K ($\Gamma_{D_2}^{div} = 10^{22}\ m^{-2}s^{-1}$ corresponds to $n_{D_2}^{div} = 3 \cdot 10^{19}\ m^{-3}$). Like the radiated power, the neutral flux density is provided for the feedback transputer system with 2.5 ms temporal resolution during a discharge.

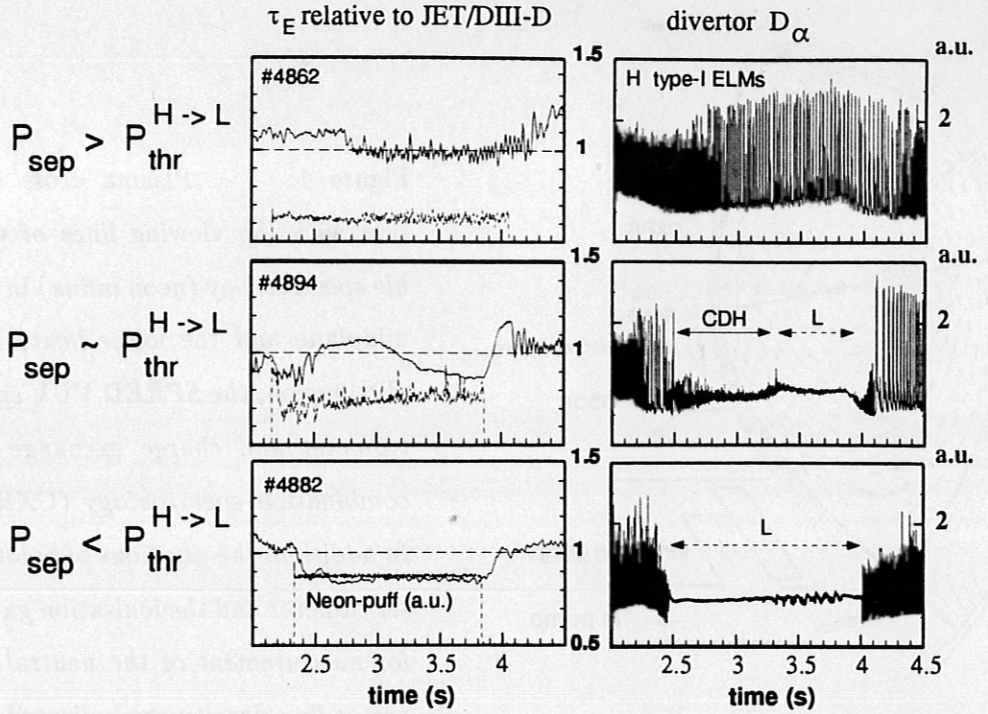

Figure 2: *Global energy confinement normalized by the value predicted by the JET/DIII-D H-mode scaling [11], neon valve fluxes and divertor D_α emission for 3 discharges with different radiation levels. $P_{heat} \approx 7.5$ MW, $I_p = 1$ MA, moderate additional D_2-puffing, # 4862, 4894 with ion ∇B drift towards, # 4882 away from the X-point. The radiated power fraction is about 55 % without Ne-puffing, 80 % during moderate puffing (# 4862) and 95 % at the H→L transition in # 4894.*

Feedback control of the radiated power fraction and/or the neutral flux density in the divertor is performed for a number of discharges by the parallel multi-transputer cluster developed for an effective real-time control of various plasma parameters in ASDEX Upgrade with 2.5 ms cycle time [10]. The fractional radiated power P_{rad}/P_{heat}, as determined by the 12 bolometer line integrals and the measured heating power, is controlled by means of impurity gas injection. The divertor neutral flux density, $\Gamma_{D_2}^{div}$, is adjusted via the injection of D_2 gas into the main chamber.

3 General behaviour of high-power discharges with neon injection

3.1 Variation of the separatrix power flux by neon puffing

The behaviour of energy confinement and divertor D_α emission from three discharges with neutral injection heating of 7 MW and different impurity injection levels is shown in Fig. 2. The divertor shows gas-bag behaviour for these experiments, i. e. the outer divertor chamber remains closed for neutral hydrogen even between ELMs. This finding is based on fast divertor D_α measurements as well as on the Γ_{D_2} flux derived from the ionization gauge which both indicate no visible decay of the divertor neutral D_2 flux density between ELMs. The relevant quantity for the desired reduction of power flow to the target plates is the total radiated power, $P_{rad}^{tot} = P_{rad}^{main} + P_{rad}^{div}$. P_{rad}^{div} is the radiated power emitted below the X-point in the lower single-null configuration. The main plasma radiation $P_{rad}^{main} = P_{rad}^{bulk} + P_{rad}^{SOL}$ is split up into fractions emitted from within the separatrix and from the scrape-off layer. The spatial distribution of the radiated power for a case with $P_{rad}^{tot}/P_{heat} = 0.8$ is shown in Fig. 3. The peaking of the radiated power density in the X-point/divertor region is mainly attributed to the intrinsic impurities, which typically give rise to radiation amounting to 50 % of the total heating power without additional gas injection. With neon injection, the emission profile develops a more uniform layer around the boundary region of the plasma. Measurements of various VUV lines with the SPRED spectrometer reveal that the intensities of the intrinsic (C, O) lines change only moderately during neon puffing. Since the power flow to the target plate is often drastically reduced during high-radiation conditions, the absence of a strong reduction of the carbon and oxygen fluxes is the consequence of the dominance of chemical erosion processes for these impurities [12].

The H-mode behaviour of the discharges is determined by the power flow over the separatrix: the variation of $P^{sep} = P_{heat} - P_{rad}^{bulk}$ caused by increasing the radiated power has essentially the same effect on the ELM characteristic as a reduction of the total heating power, i. e. starting with a high P^{sep}, as P^{sep} is reduced the type-I ELM frequency decreases, as P^{sep} is reduced further a transition from type-I to type-III like (CDH-) ELMs occurs, and eventually a transition to L-mode takes place. The Completely Detached High-confinement mode [13] will be described in more detail in section 6. While this general behaviour is quite evident, a moderate variation of the H→L power threshold in such experiments cannot be ruled out. Owing to the uncertainties of the bolometer deconvolution, a precise separation between bulk plasma, X-point

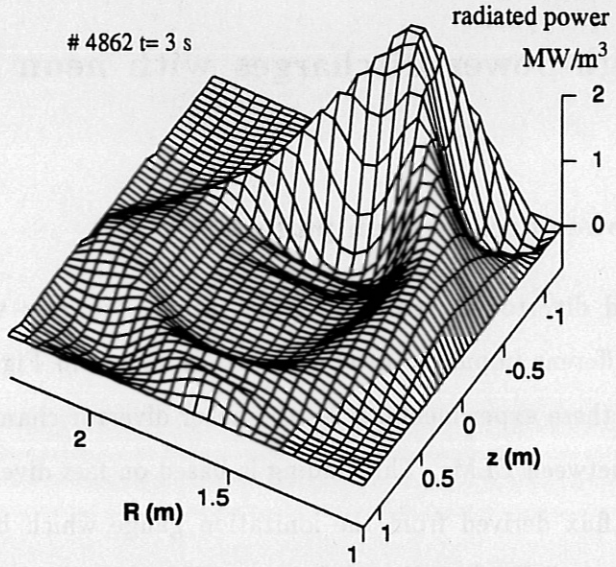

Figure 3: *Emitted power density from bolometer deconvolution for the upper discharge of Fig. 2.* P_{rad}^{tot}*= 6 MW.*

and SOL radiation is not possible, leaving some uncertainty to P^{sep} (see Sect. 5).

The global energy confinement time $\tau_E = W/(P_{tot}\text{-}\dot{W})$ observed in these discharges is shown normalized by the JET/DIII-D ELM-free H-mode scaling for the thermal energy confinement time [11]. The ELMing H-mode is seen to have τ_E equal to the predicted value, and the period with the type-III like (CDH-)ELMs has an even higher τ_E. The τ_E is calculated from the magnetics not corrected for fast ion content. However, at the plasma densities used in this work the non-thermal contribution is less than 15 % and comparable to the losses caused by the ELMs.

The impurity-forced L-mode exhibits an energy confinement time which is significantly improved in comparison to the ITER89-P scaling [14] with H reaching 1.4. Note that such discharges differ from the usual conditions in a divertor tokamak: they are L-mode discharges with heating power well above the H-mode threshold, in other words they have strong core heating with however low edge temperature. It should be reminded that improved confinement in connection with strong impurity radiation was also observed in circular limiter tokamaks [15], [16].

3.2 Variation of the deuterium flux

Deuterium puffing in the main plasma strongly influences the behaviour of radiative boundary discharges. Fig. 4 shows a comparison of two discharges with and without additional D_2 puffing and otherwise identical external parameters.

Generally in ASDEX Upgrade, deuterium puffing into H-mode discharges only leads to a mod-

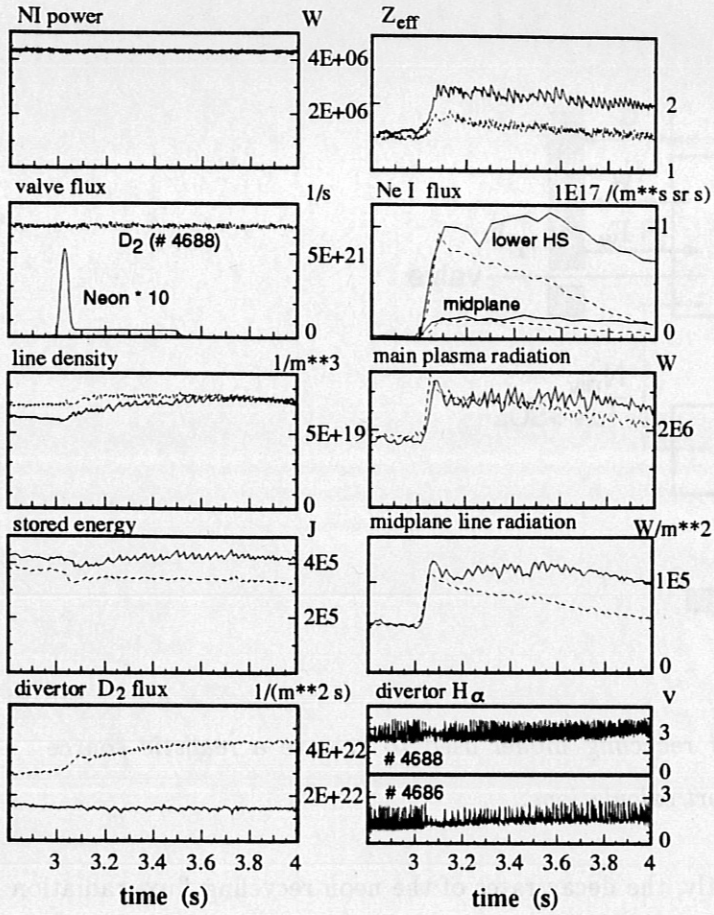

Figure 4: *Comparison of discharges with preprogrammed neon injection with (#4688, dotted lines) and without (#4686, solid lines) additional D_2 puffing and otherwise identical external parameters. Shown are the neutral beam power, gas valve fluxes, line-averaged electron density from DCN interferometry, total stored energy from magnetic equilibrium, divertor D_2 flux measured by the fast ionization gauge, line-averaged Z_{eff} derived from bremsstrahlung measurements, NeI photon fluxes in the midplane and lower divertor region, total main plasma radiation and line-averaged midplane radiation and H_α emission from the outer divertor. I_p= 0.8 MA.*

erate increase of the line-averaged density, which is to first order determined by the plasma current and scales almost linearly with I_p [17]. The D_2 puffing results in a higher edge density, a slight increase of the type-I ELM frequency, a reduction of the impurity content in the main plasma and increased radiation, in particular in the X-point/divertor region. Accompanying these beneficial effects is a slight reduction in the energy confinement time, as has been observed on several tokamaks. The experimental parameter which is most affected by the deuterium puff is the neutral D_2 flux in the divertor, which increases almost offset-linearly with the magnitude of the applied gas puff. This behaviour is easily explained by the necessary argument for steady-state conditions: the constancy of the electron density requires an equilibrium between fuelling and pumping. Neglecting the effect of wall pumping, the injected gas is completely removed by the turbomolecular pumps, their effective throughput being nearly proportional to the divertor neutral D_2 flux density. Therefore, a D_2-puff in the main chamber essentially inflates the divertor volume with D_2 gas. The different D_2 neutral conditions produce significantly different results

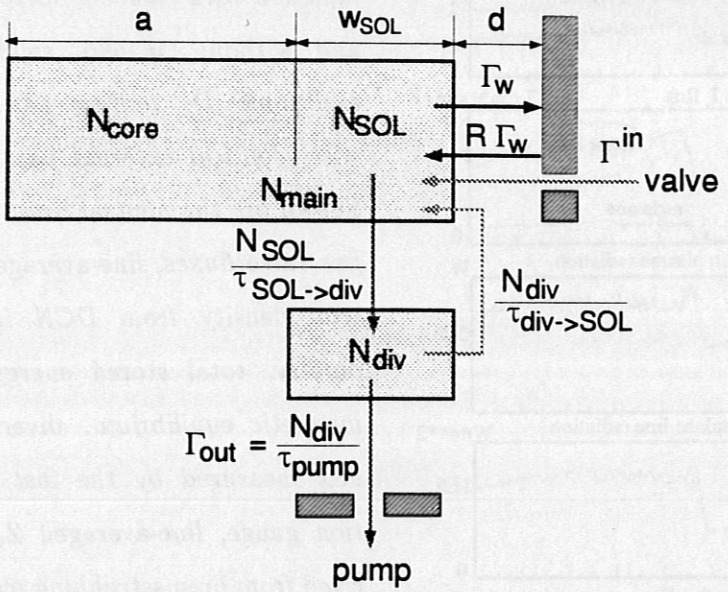

Figure 5: *Sketch of the simplified recycling model used to achieve a realistic source function for the radial impurity transport calculations.*

for discharges with neon injection: Firstly, the decay rates of the neon recycling flux, radiation and Z_{eff} are faster by more than a factor of 3 for the discharge with the higher divertor neutral flux density Γ_{D_2}. Secondly, the increase of Z_{eff} is much smaller for the discharge with higher Γ_{D_2}, despite the fact that the injected amount of neon is the same. However, the radiated power is the same in both cases, indicating that it is related to the neon influx rather than to the neon content.

The bolometer deconvolution shows that the relative increase of the midplane radiation with neon injection is higher than that of the total radiated power. This is due to the different spatial radiation profiles of the intrinsic impurities (C, O) in comparison to neon. While the radiation profile without neon injection is peaked in the X-point region, neon adds a more equally distributed radiative mantle around the whole plasma.

4 Pumping and particle balance

A prerequiste for the feedback control of a radiative plasma mantle is the ability to pump the injected species. In the following, we describe the pumping behaviour using a simplified chamber model of the particle balance. Its basic properties are outlined in Fig. 5. A species

i (e.g., neon) is puffed via the valve into the main chamber with a flux Γ_i^{in}. Owing to various transport processes, the particles are distributed between main plasma and divertor chamber. The particle fluxes between scrape-off layer and divertor are treated by the simplified ansatz of empirical loss times which are determined from experimental data (the details of core transport and wall recycling will be introduced in the next section). Particles entering the SOL are lost to the divertor with a decay time $\tau_{SOL \rightarrow div}$. Particles in the divertor either escape to the main chamber with the time constant $\tau_{div \rightarrow SOL}$ or are pumped out within the pumping time τ_{pump}. The pumping speed S of the 14 turbomolecular pumps situated near the outer divertor decreases with the mass of the pumped species from $S_{D_2,He} = 13\ m^3/s$ to $S_{Ne} = 6.9\ m^3/s$ in the limiting case of molecular flow. With increasing gas density the pumping speed increases up to $S_{D_2,He} = 17.6\ m^3/s$ at $n_{D_2,He} = 2 \cdot 10^{20}\ m^{-3}$ as obtained from an *in situ* calibration. In the other limiting case of laminar flow conditions ($n > 1.5\ 10^{21}\ m^{-3}$) neon and deuterium are pumped with the same pumping speed, which for low neon concentrations equals the pumping speed for deuterium. For the investigated parameter range we estimate that the pumping speed for neon increases offset-linearly up to $S_{Ne} = 11\ m^3/s$ at the highest divertor densities. Since no in situ calibration of the neon pumping speed in the presence of a D_2 flow was available, this value has to be regarded as more uncertain in comparison to the D_2 values. The pumping speed and pumping time are connected via the pumped divertor volume $V^{div} = S_i \cdot \tau_{pump}$.

Assuming complete recycling at the wall, R=1, the effective particle confinement time τ_p^* considerably exceeds the main plasma particle confinement time, τ_p. τ_p^* only depends on the pumping time and the relative populations in the main plasma volume N^{main} and in the divertor volume N^{div}:

$$\tau_p^* = \frac{V^{div}}{S} \cdot (1 + \frac{N^{main}}{N^{div}}) \qquad (1)$$

Measurements of the 1/e-decay time $\tau_i^{1/e}$ of the recycling flux after the injection phase give a reasonable estimate of τ_p^* and allow to determine the partition of the impurity species i between the main and divertor volumes:

$$\frac{N_i^{main}}{N_i^{div}} = \frac{S_i \cdot \tau_i^{1/e}}{V^{div}} - 1 \qquad (2)$$

With the known volume V^{main} the compression factor (ratio of divertor neutral density and bulk plasma ion density) is given by:

$$C_i = \frac{n_i^{0,div}}{n_i^{ion,main}} = \frac{V^{main}}{S_i \cdot \tau_i^{1/e} - V^{div}} \quad . \qquad (3)$$

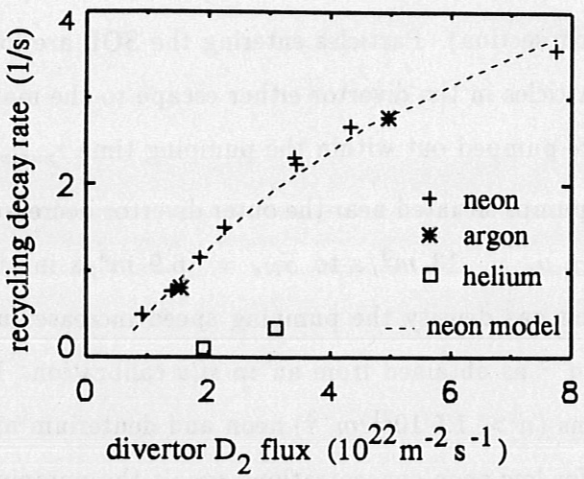

Figure 6: *Recycling 1/e decay rates (inverse effective particle confinement times) from several discharges after Ne or Ar puffing versus divertor D_2 flux. The dashed line shows the prediction of the chamber model for neon for the offset-linear increase of the neon pumping speed and the assumption of a quadratic lengthening of divertor retention with $\Gamma_{D_2}^{div}$. P_{heat}= 4-6 MW, ion ∇B drift towards the X-point.*

A further quantity of interest is the enrichment factor η_i of the species i,

$$\eta_i = \frac{(p_i^0 \;/\; 2p_{D_2}^0)^{div}}{(n_i \;/\; n_e)^{main}} = C_i \cdot \frac{n_e^{main}}{2n_{D_2}^{0,\,div}} \quad . \tag{4}$$

η_i is a measure for the compression of the species i relative to that of the working gas (deuterium). The various parameters introduced above are derived from experimental data taken from neon-injection experiments into H-mode plasmas with type-I ELMs. The analysis of the decay time of the recycling flux as shown in Fig. 4 yields information about the effective particle confinement time τ_p^*, the impurity compression C_i and the enrichment factor η_i.

The variation of a number of experimental parameters revealed that the divertor neutral D_2 flux is the leading parameter to determine the exhaust rate (atoms/s) of noble gases in deuterium plasmas. The neutral divertor flux density $\Gamma_{D_2}^{div}$ is controlled by D_2 fuelling in the main plasma. After a transient phase with active wall pumping, $\Gamma_{D_2}^{div}$ approaches a value which is proportional to the injected flux $\Gamma_{D_2}^{in}$. Fig. 6 shows recycling decay rates $1/\tau^{1/e}$ for neon and argon versus the divertor D_2 flux. The exhaust rate increases with the divertor D_2 flux but the slope decreases with higher values of the D_2 flux when the majority of neon atoms is already situated in the divertor volume. Not much difference is seen in the decay rates of neon and argon, but the exhaust rate obtained for 2 discharges with helium injection is much slower, although the accelerating effect of a high divertor D_2 flux on pumping is also observed for helium. Beside the beneficial effect of D_2 puffing on the impurity pumping, a moderate degradation of the energy

confinement occurs, which amounts to about 20 % over the parameter range covered in Fig. 6. The large variation of the effective particle confinement time by a factor of 7 shown in Fig. 6 cannot be explained by the increase of the pumping speed which changes at most by a factor of 1.5 to 2 as has been described above. It is mainly determined by the large variation of the impurity distribution between the main plasma and the divertor volume (second factor in Eq. 1). With a further simplified chamber model that handles the transport between core and SOL volume in the same manner as has previously been explained for the transport to and from the divertor the measured 1/e-times and the connected change of the divertor population can readily be understood by a variation of the ratio of the time constants $\tau_{SOL \rightarrow div}/\tau_{div \rightarrow SOL}$. A decrease of this ratio causes a decrease of the ratio N^{main}/N^{div} leading to a faster decay rate. The dashed curve in Fig. 6 shows the result from such a model calculation where the assumption was used that the divertor retention time $\tau_{div \rightarrow SOL}$ increases with the square of the divertor D_2 flux density while the other time constants are kept constant. An effective divertor volume $V^{div} = 3\ m^3$ is used in approximate accordance with the real geometrical situation in the torus. The measured decay rates are well reproduced over a broad parameter range. In principle, the observed experimental behaviour could also be explained by a reduction of $\tau_{SOL \rightarrow div}$ with increasing Γ_{D_2}. The comparison with other experimental observations, like the early increase of the neon density in the main plasma after the opening of the valve, revealed that the retention time indeed is the parameter which predominantly varies with Γ_{D_2}.

Fig. 6 allows determination of the compression and enrichment factors for the parameter range shown. We will restrict the analysis to neon injection experiments, where a broad experimental database exists. As effective main plasma volume we use $V^{main} = 15\ m^3$, to which the volume enclosed by the separatrix contributes with 13 m^3. Various neon pumping properties obtained from the decay time analysis for 2 discharges with low and high divertor neutral density are summarized in Table 1. The high value of η_{Ne} for the case with strong gas puffing expresses the fact that the compression of neon considerably exceeds the corresponding deuterium compression for these experimental conditions.

While no direct measurement of the neon divertor density is available at present, the analysis of steady-state conditions give another indication for the compression of neon in the divertor volume. In a discharge with feedback controlled radiated power and divertor neutral density steady-state conditions are achieved 1 s after the start of the neon injection and lasted for a duration of 1.6 s. As a consequence, the pumping rate balanced the injected neon flux of

discharge	$n_{D_2}^{div}$ (10^{20} m^{-3})	$\overline{n}_e^{main}$ (10^{19} m^{-3})	S_{Ne} (m^3/s)	$\tau_{Ne}^{1/e}$ (s)	C_{Ne}	η_{Ne}
4686	0.46	7	8	1.3	2	1.5
4688	1.4	7.3	10	0.37	21	5.6

Table 1: *Pumping properties for 2 discharges with different divertor neutral density. The compression and enrichment factors are calculated from Eqns. 3 and 4. The high values obtained for # 4688 are subject to increased uncertainty due to partial cancellation of* V^{div} *and* $S_{Ne} \cdot \tau_{Ne}^{1/e}$ *in the denominator of Equ. 3.* P_{heat}*= 5 MW,* I_p*= 0.8 MA.*

on average $9.5 \cdot 10^{19}$ atoms/s. Dividing this volume by the pumping speed S_{Ne} yields the corresponding density in front of the pump $n_{Ne} = 9 \cdot 10^{18}\ m^{-3}$. This density, however, cannot be present in the whole plasma volume because 1 s after the start of the neon puff only 60% of the neon atoms that would be required have been injected into the vessel. Therefore, the observed behaviour can only be understood by assuming a compression of neon in the divertor volume. From the measured divertor D_2 flux the chamber model calculates the relevant compression parameters for the pumping characteristics $C_{Ne} = 16$, $\eta_{Ne} = 5.3$, $\tau_{Ne}^{1/e} = 0.38\ s$. A decay time analysis is not possible for the steady state discharge because the neon and D_2 feedback were switched off simultaneously leading to a fast change of the divertor density during the neon decay.

The same procedure was applied to the discharge with helium puff indicated in Fig. 6 by the data point at $\Gamma_{D_2} = 3.1 \cdot 10^{22}\ m^2/s$. For experimental conditions slightly different from those of Table 1 (I_p= 1 MA, P_{heat}= 7.5 MW), we obtain for these relatively low divertor D_2-flux conditions C_{He}=0.35 and η_{He}=0.15. At present, we can give no comprehensive explanation of the huge difference between the neon and helium compression. Detailled modelling of this experimental situation with the B2/EIRENE code package is under way.

The interpretation of the measured decay rates of the recycling flux may be affected by a possible wall pumping of the noble gases, as reported, e.g. from TORE SUPRA [18]. For the case of helium injection in ASDEX Upgrade, the contribution of wall storage to the decay was investigated by uncoupling 13 of the 14 turbopumps. No change of the helium recycling level was observed over 2.5 s after a helium puff for experimental conditions similar to those where a decay time $\tau^{1/e}$ of 2.9 s was measured with all pumps active. Therefore, a long-lasting wall

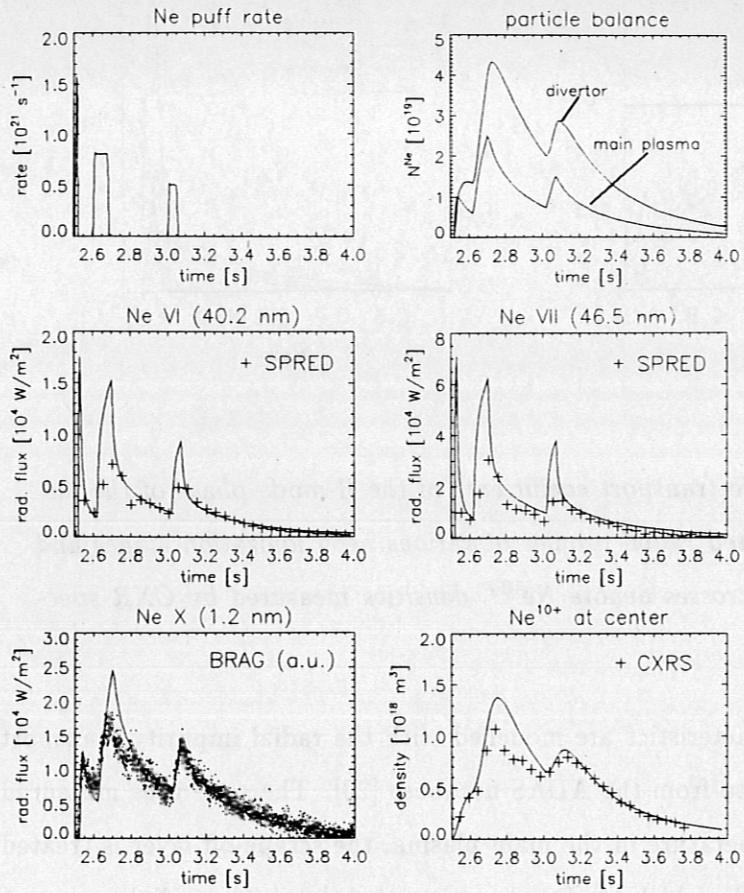

Figure 7: *STRAHL modelling of a discharge with 3 neon pulses and strong D_2 puffing. The discharge is in the H-mode except a short impurity-forced H→L transition at t=2.7 s. The solid lines represent the prediction of the radial transport calculation using the simplified chamber recycling model. #4286, I_p = 0.8 MA, P = 6.5 MW, $\Gamma_{D_2}^{div} = 8 \cdot 10^{22}\ s^{-1}$, $\overline{n}_e = 8 \cdot 10^{19}\ m^{-3}$.*

pumping of helium can be excluded. The storage of neon at the wall seems also to be a small effect for parameters typical of this study. In the case of argon injection a very slow penetration into the plasma is observed, which may be partly due to long wall residence times of argon. Measurements with reduced pumping speed are not available for neon and argon.

We conclude, that the chamber model for main plasma and divertor is sufficient to describe the temporal evolution of the neon recycling flux, which is a necessary input for the calculation of the neon emissivity using the impurity transport code STRAHL as described in the next section. The complicated physics of the neutral gas compression, which is not fully understood yet, is concealed in the empirical time constants $\tau_{SOL \to div}$ and $\tau_{div \to SOL}$, which are derived from experimental data.

5 Modelling of bulk impurity transport and emission

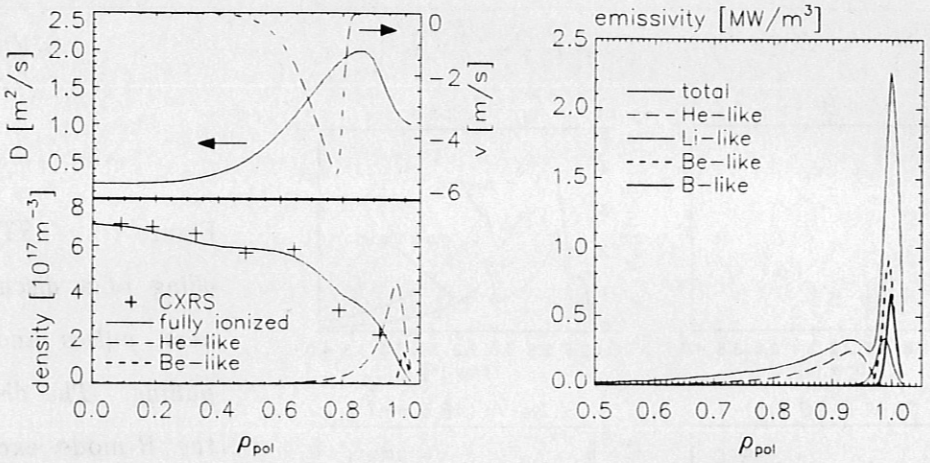

Figure 8: *ELM-averaged particle transport coefficients of the H-mode phase of the discharge shown in Fig. 7 and calculated radial profiles of various neon ionization stages and emissivity profiles at t= 3 s. The crosses denote Ne^{10+} densities measured by CXR spectroscopy.*

Impurity profiles and emission characteristics are modelled with the radial impurity transport code STRAHL [19] using atomic data from the ADAS database [20]. The code uses measured profiles of electron density and temperature in the main plasma, the scrape-off layer is treated in a simplified way using decay lengths which are fitted to measured data. The radial transport equations of impurity particles are solved in 1-d geometry using an ansatz of anomalous diffusivities and radial drift velocities, a full neoclassical treatment of particle transport can be switched on if desired. An essential feature of the modelling is the empirical description of the recycling and pumping using the simple chamber model for recycling and pumping as discussed in the previous section and shown in Fig. 5. The particle balance as described by the chamber model supplies the absolute neutral source as input for the 1-d core transport calculations, providing a self-consistent description of the particle content and its temporal development on the basis of the calibrated valve flux and the pumping speed of the turbomolecular pumps.

The particle transport coefficients for the central part of the main plasma are experimentally determined from the time evolution of neon profiles measured by CXR spectroscopy. The diffusion coefficient D and radial drift velocity v are taken directly from linear regression analysis of the time behaviour of normalized densities versus the normalized fluxes at various radial positions r [21] following a short puff of neon:

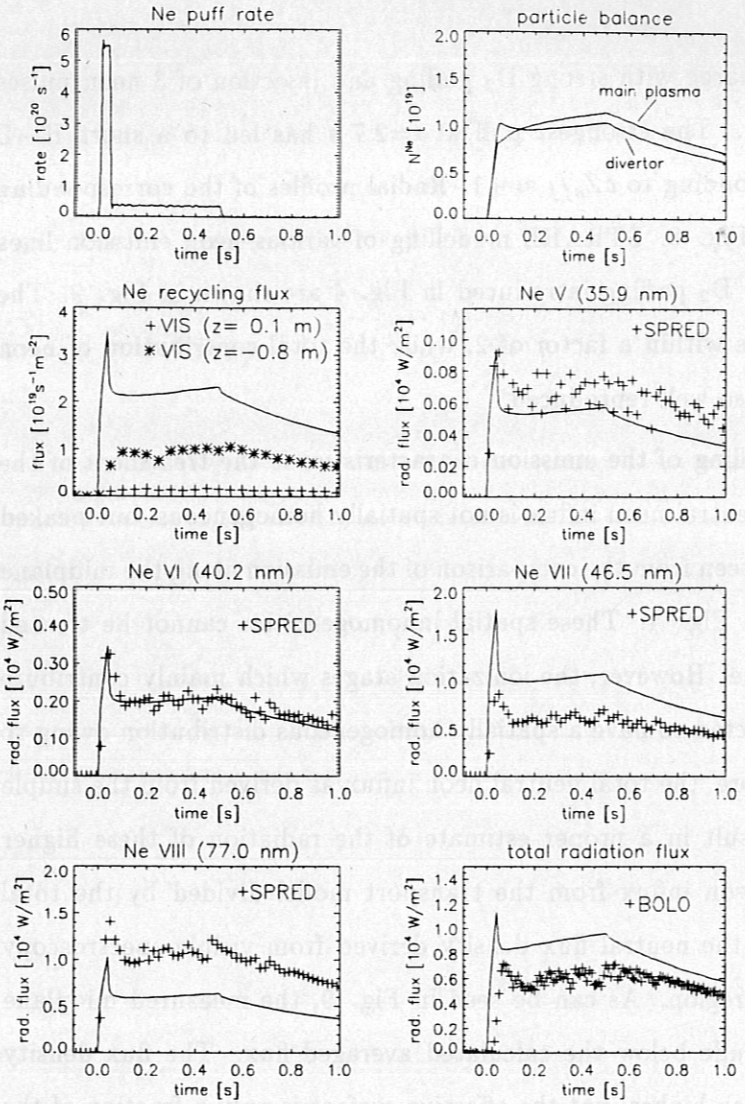

Figure 9: *STRAHL modelling of the H-mode discharge without additional D_2 puffing (#4686) shown in Fig. 4.*

$$\frac{\Gamma_i(r,t)}{n_i(r,t)} = -D(r) \cdot \frac{\nabla n_i(r,t)}{n_i(r,t)} + v(r). \qquad (5)$$

This analysis in principle allows calculation of the transport coefficients only in the source-free region, i. e. in our case in the inner part of the plasma where the hydrogen-like neon density is negligible. To extend the useful range somewhat to larger minor radii, the Ne^{10+} source function is calculated from the transport model and supplementary inserted into Eq. 5 in order to improve the values of v (D is less affected) in the source region. The transport coefficients outside $\rho_{pol} = 0.6$ are taken from the similar analysis of helium-puffing experiments under comparable experimental conditions (the central transport parameters derived for helium and neon are equal). Owing to the long integration time of the CXRS diagnostic in comparison to the ELM frequency, these transport coefficients represent an average of the dynamics of the ELM transport.

Fig. 7 shows an example for a discharge with strong D_2 puffing and injection of 3 neon pulses to obtain large temporal variations. The strongest puff at t=2.7 s has led to a short H→L transition at a neon density corresponding to $\delta Z_{eff} \approx +1$. Radial profiles of the corresponding transport coefficients are shown in Fig. 8. STRAHL modelling of various neon emission lines for the discharge without additional D_2 puffing introduced in Fig. 4 are shown in Fig. 9. The agreement with the measurements is within a factor of 2, while the total contribution of neon to the bolometric measurement is also well reproduced.

Somewhat problematic in the modelling of the emission characteristics is the treatment of the neutral neon source function. The neutral neon influx is not spatially homogeneous, but peaked around the X-point region as can be seen from the comparison of the emission along the midplane and lower viewing lines as shown in Fig. 4. These spatial inhomogeneities cannot be treated with the 1-d impurity transport code. However, the ionization stages which mainly contribute to the neon radiated power are expected to have a spatially homogeneous distribution owing to the rapid parallel transport. Therefore, the total neutral neon influx as derived from the simple chamber recycling model should result in a proper estimate of the radiation of these higher ionized states. The total neutral neon influx from the transport model divided by the total plasma surface is also compared to the neutral flux density derived from visible spectroscopy in the midplane and lower divertor region. As can be seen in Fig. 9, the measured midplane recycling flux is an order of magnitude below the calculated averaged flux. The flux density above the X-point appears to be much higher, but the effective surface is only a fraction of the total plasma surface. Therefore, the apparent total neon influx is only partly established by the spectroscopic influx measurements. A possible explanation for this fact may be found in 'hidden' recycling regions, like limiter or baffling structures on the low-field side, the presence of a very high neutral influx just around the X-point, or the significant contribution of neon ions backstreaming from the divertor. Generally, the magnitude of the total emitted power is closely coupled to the neutral influx measured above the X-point region. This is shown in Fig. 10, where the NeI photon flux above the X-point is compared to the intensity of a NeVIII line and the total increase of the main plasma radiation. While the relation between the NeI and NeVIII radiation is approximately linear, the increase of the total radiation is slightly slower than that of the NeI flux. Such moderate relative variations of photon fluxes are expected from the individual changes of the effective S/XB values [22] of different spectral lines owing to the variation of the edge plasma parameters.

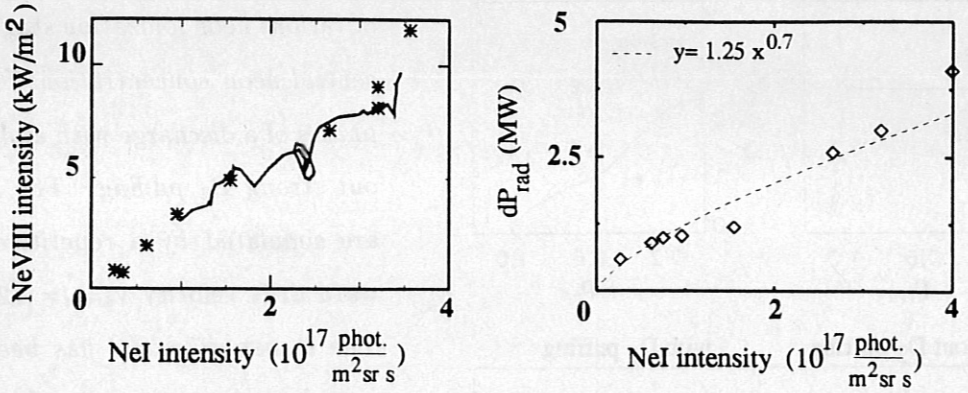

Figure 10: *Measured NeI photon flux, representing the neutral neon recycling flux integrated along the lower line-of-sight shown in Fig. 1 versus the NeVIII midplane radiation during the temporal evolution of a single discharge (solid line) and for selected timepoints of various discharges with different experimental parameters. The right picture shows the increase of main plasma radiation as a function of the NeI flux. Regression analysis reveals the dependence* $dP_{rad} \propto \Gamma_{NeI}^{0.7}$.

So far, we have only treated the impurity profiles averaged with respect to ELM activity. Based on fast measurements of OVIII and CVI lines with a Bragg spectrometer, a simple 1-d radial transport model has been developed which takes into account fast changes of transport coefficients in the edge region. The ELM activity is described by the repetitive occurence of an outward drift velocity v_{drift}= 12 m/s. With the transport parameters adjusted to measurements of the intrinsic impurities C and O, the prediction of the model for various neon emission lines is shown in Fig. 11 for two phases of a discharge with and without strong D_2 puffing. This particular discharge was preferred to those of Fig. 4 due to the better measurements of plasma profiles available. Since no neon injection was applied the prediction of Fig. 11 is valid only in the trace amount limit. The model clearly reproduces the observed higher radiative capability of neon with strong D_2 puffing: While the line emission of various ionization stages remains comparable (the neutral influx was set equal and constant for both cases shown), the central neon concentration is lower by a factor of 2.4 with D_2 puffing. This behaviour is mainly attributed to the much higher edge density for these conditions, leading to an outward shift of the emitting shells. The impurity screening takes place smoothly over the various ionization stages. The emission strengths of the corresponding spectral lines on average do not decrease due to the fact that electron impact excitation is more effective for these higher density / lower temperature conditions. The slight increase of the ELM frequency with D_2 puffing has a minor

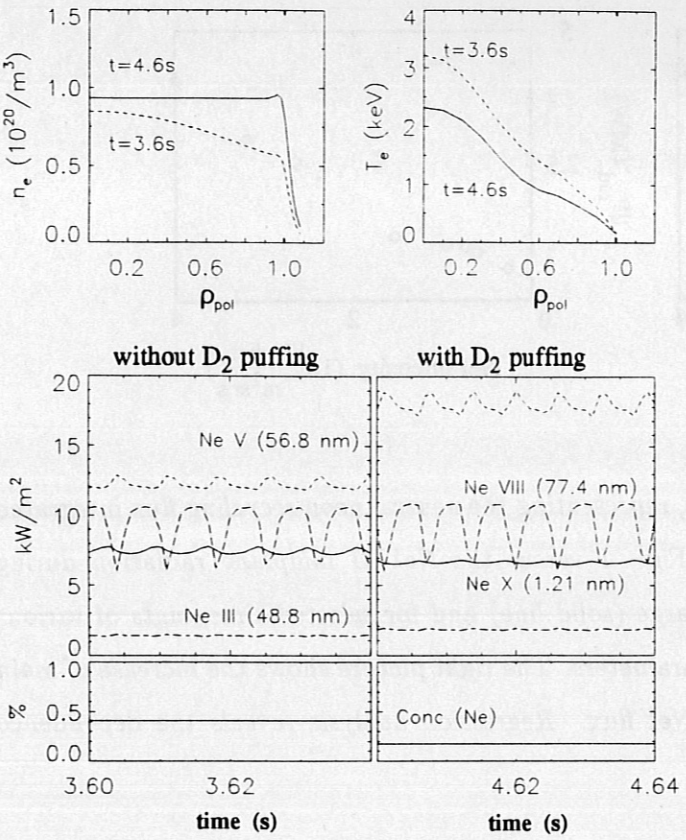

Figure 11: *Predicted radiation of various neon ionization stages and central neon concentrations for two phases of a discharge with and without strong D_2 puffing. The ELMs are simulated by a repetitive outward drift velocity v_{drift}= 12 m/s. The transport model has been adjusted to the temporal evolution of the intrinsic impurities C and O measured with a Bragg spectrometer. The T_e and n_e profiles correspond to a situation without neon injection, therefore the calculated neon emissivities are valid in the trace impurity limit.* $\Gamma_{D_2}^{div}$= *1.7 and 5.7* $\cdot 10^{22}$ $m^{-2}s^{-1}$, *respectively.*

contribution to the observed impurity screening, in contrast to the situation of a heating power scan where the ELM frequency varies considerably.

The strong impact of impurity screening on the emission capability of neon during D_2 gas puffing is further elaborated in Fig. 12. The 'figure of merit' for radiative scenarios, the additional radiated power per unit Z_{eff} increase, almost linearly increases with the divertor D_2 flux, which acts here as a measure of the main plasma edge electron density. On the other hand, the parameter $\delta Z_{eff} \cdot \Gamma_{D_2}^{div\,0.8}$ well describes the additional radiated power, as shown in the right picture of Fig. 12.

At this place, it should be mentioned explicitly that there exist some limitations for the interpretation of the results obtained by the procedures described above. Firstly, the fact that the SOL plasma is treated in a very crude way leads to some uncertainty in the emission strength of lines from the low ionization stages residing predominantly outside the separatrix. Secondly, the spatial distribution of the radiation, namely that part emerging from the X-point region, is not included in the description. However, as long as our main interest is in the behaviour of those emission lines which carry most of the power flux, these deficiencies are not essential. The deconvolved emissivity profiles from bolometry are typically not accurate enough to determine,

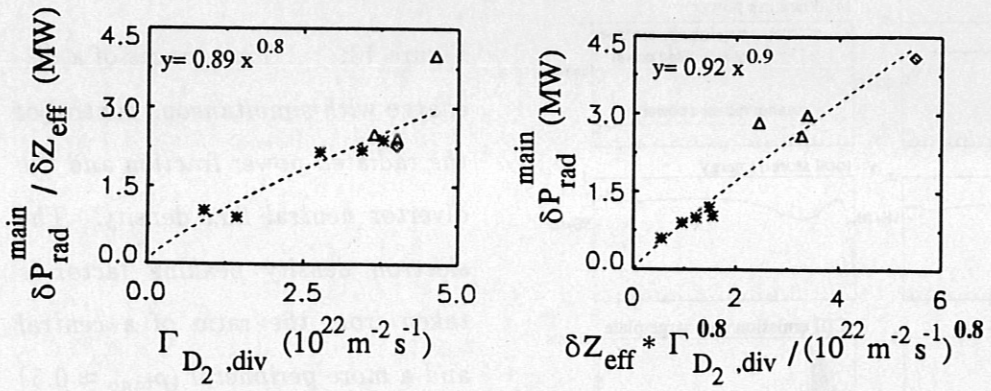

Figure 12: *Radiative capability $\delta P_{rad}/\delta Z_{eff}$ for neon versus the neutral D_2 flux in the divertor for H-mode discharges. Stars denote type-I ELMy H-modes, triangles for CDH-modes and diamonds represent the impurity-forced L-mode. The right picture shows the measured increase of the radiated power versus the quantity $\delta Z_{eff} \cdot \Gamma_{D_2}^{0.8}$, which is found to be a good measure for the power radiated by neon. The δZ_{eff} is taken from the chamber model analysis of the neon balance.*

e.g., the exact fraction of power emitted inside the separatrix. This quantity, which is thought to be essential for the H-mode behaviour, is better represented by the prediction of the 1-d radial impurity transport calculations. For the experimental conditions typical of this paper, about 2/3 of the main chamber radiation is emitted inside the separatrix. While the surface-averaged neutral influx is well described by the simple chamber recycling model, the spatial neutral influx pattern as well as the detailed X-point and divertor emission profile await modelling with coupled fluid and Monte-Carlo codes, like the B2/EIRENE package.

6 Energy confinement aspects and complete detachment

Because of the strong influence of the neutral divertor flux on the pumping and emission characteristics of radiative mantle discharges, feedback regulation of this quantity has been incorporated into the control system of ASDEX Upgrade. Fig. 13 shows the temporal development of various experimental parameters for a discharge with radiated power and divertor neutral flux feedback control exhibiting the completely detached high confinement (CDH-) mode with more than 90 % radiated power fraction. The small, high-frequency CDH-ELMs are buffered by the divertor plasma, as can be seen from the CIII emission which vanishes in front of the target plate. Langmuir probe measurements indicate almost complete detachment at the strike point, while further outside partial attachment is observed at low power flux levels. Thermo-

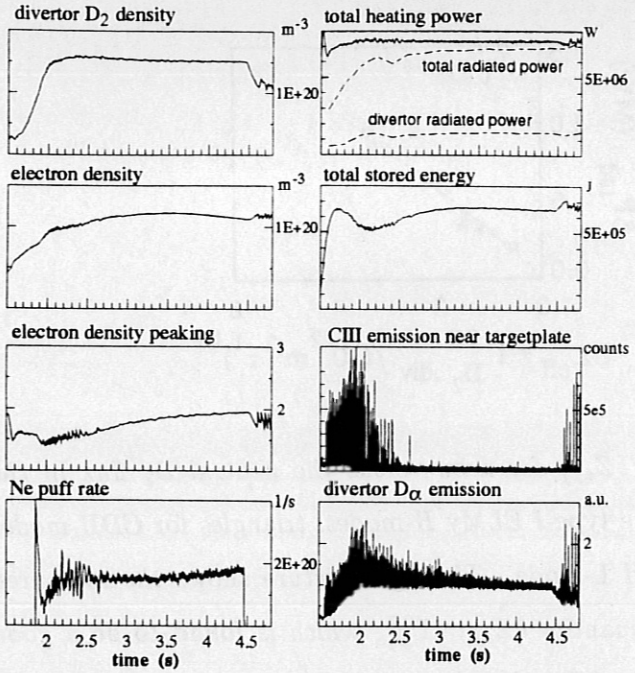

Figure 13: *Time traces of a discharge with simultaneous control of the radiated power fraction and the divertor neutral flux density. The electron density peaking factor is taken from the ratio of a central and a more peripheral ($\rho_{tang} \approx 0.5$) DCN interferometer chord integral, with a length ratio $l_{central}/l_{peripheral}$ =1.2. The CDH-mode is achieved in the time interval from 2.7-4.5 s. # 5028, I_p= 1 MA .*

graphic measurements of the power density at the outer target plate shown in Fig. 14 reveal no burnthrough of ELMs and a power level below 1 MW/m^2 during the CDH-phase. During the type-I ELMy H-mode before neon injection, a narrow energy deposition layer is seen in between ELMs, while the type-I ELMs exhibit a broad deposition profile. The global signature of the CDH-ELMs, in particular the power dependence, is type-III like. Such complete detachment preserving high H-mode confinement as obtained with neon injection could not be achieved with deuterium puffing alone [13].

The temporal development of the CDH-phase is accompanied by a moderate peaking of the electron density profile, by the disappearance of the sawteeth and by the emergence of a strong m=1 mode in the plasma center. It is speculated that this m=1 mode stops the further evolution of density peaking in the center and therefore prevents impurity accumulation which is often observed in connection with electron density peaking [23]. The occurence of density peaking with improving energy confinement, particularly connected with the reduction of the separatrix power flow by impurity injection, was also observed during investigations of the IOC regime in ASDEX [24].

The most unambiguous characterisation of the CDH-ELMs is given by the analysis of CII emission in front of the target plates. Fig. 15 shows the intensity distribution of the CII emission measured with near-tangential viewing lines above the outer target plate for two discharges with CDH-mode and with type-I ELMs. The divertor D_α emission and power fluxes from Langmuir probes are shown for comparison. The CII radiation in the CDH-phase exhibits a broad and

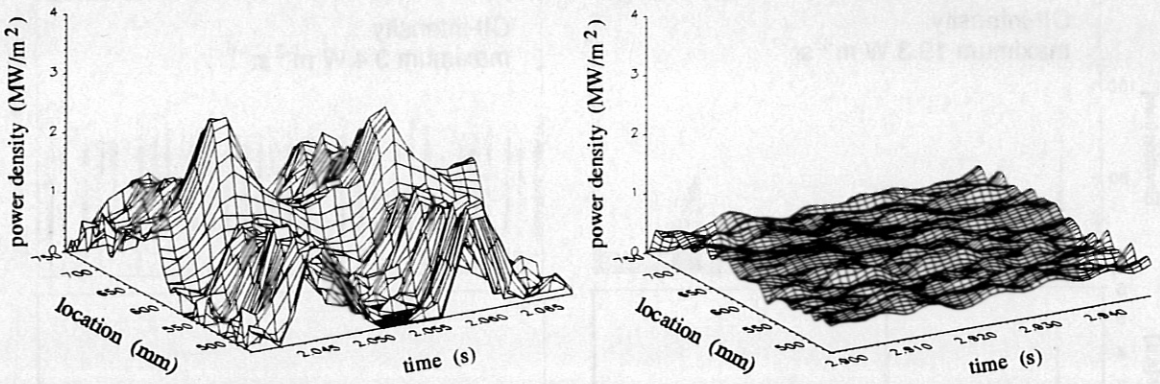

Figure 14: *Power density at the outer target plate from thermography measurements for two time intervals of the discharge # 5028 shown in Fig. 13. Shown are two time-slices of the type-I ELMy H-mode before and during the CDH phase with neon injection. The strike point of the separatrix is situated approximately in the middle of the 0.3 m spatial interval shown .*

nearly uniform emission characteristic over about 80 mm above the target plate. The type-I ELMs, in contrast, show intense emission localized just in front of the target plate.

The analysis of a number of discharges with various radiation levels revealed that the latter hardly affect the energy confinement time. Slight degradation of confinement is caused by deuterium puffing, as summarized in Fig. 16. The CDH-mode again obtains τ_E values slightly higher than the prediction of the JET/DIII-D scaling. With the exception of the data point at high D_2 flux level, the impurity-forced L-mode also exhibits good energy confinement behaviour, with τ_E values typically 25 % below the corresponding H-mode values.

7 Conclusions

We have shown, that the significant power flux reduction to the divertor plates by injecting impurities is compatible with stable operation in the ASDEX Upgrade tokamak. The power flow to the divertor plates can be reduced to values below 1 MW/m^2 while preserving the H-mode and without energy confinement degradation.

Deuterium puffing in the main plasma affects the plasma behaviour in various ways. The divertor retention for noble gases is improved when the neutral deuterium flux in the divertor is increased

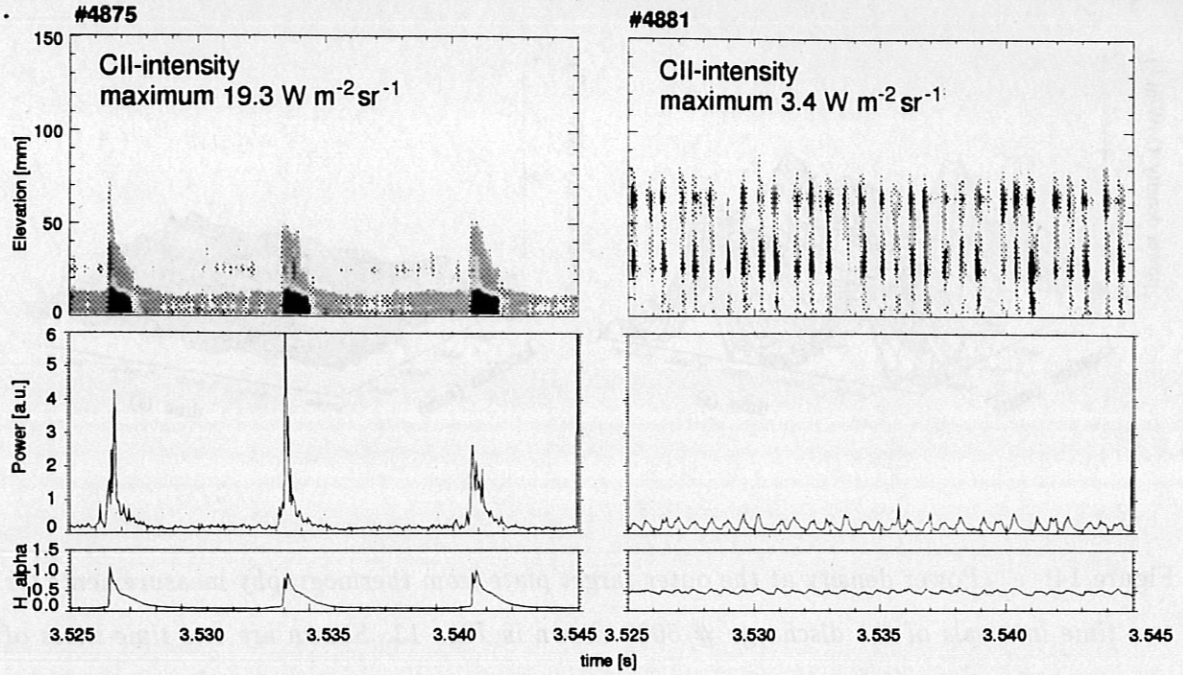

Figure 15: *Comparison of CII emission in front of the divertor plate, Langmuir probe measurements at the plate and divertor D_α emission for a discharge with type-I ELMs (left) and a discharge with CDH-ELMs (right).*

by puffing deuterium in the main chamber. According to our present understanding, this particle stream counteracts the thermal forces which tend to drive impurities out of the divertor towards the midplane, and the strength of the thermoforces is reduced by the lower temperature gradient along the field lines because the separatrix temperature is lowered during gas puffing. The better divertor retention leads to a higher exhaust rate of the injected impurities, facilitating radiation feedback operation. While the effect on retention is observed to be qualitatively similar for helium, neon and argon, the absolute value of the retention time constant is much higher for the two heavier species.

Another effect of an increased neutral flow against the main plasma is a higher radiated power per impurity ion contaminating the plasma bulk. This is attributed to the reduced edge particle confinement time and lower temperatures due to higher ELM activity in combination with better impurity screening by the higher edge density.

In addition to the positive effects mentioned above, strong D_2 puffing leads to a moderate deterioration of the global energy confinement time probably due to the ELM frequency increase. However, the choice of D_2 flow offers a huge amount of flexibility for the operation of a divertor

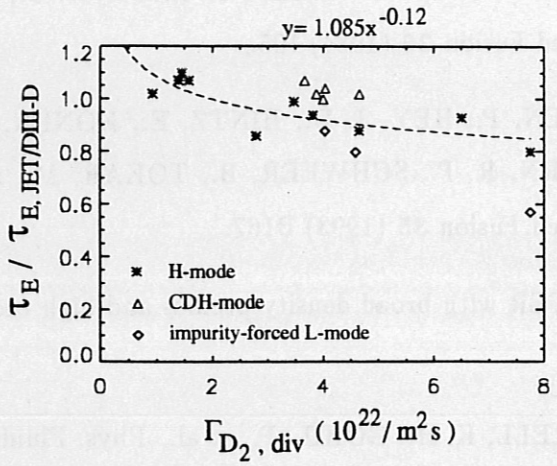

Figure 16: *Energy confinement normalized to the prediction of the JET/DIII-D H-mode scaling for discharges with various divertor neutral flux densities and radiation levels (P_{rad}/P_{heat} = 0.55-0.95) due to neon injection. The radiation level hardly affects τ_E in type-I ELMy H-mode.*

tokamak with radiating boundary: given a certain amout of radiated power flux, better plasma purity can be exchanged for a moderate reduction of energy confinement. When the power flow over the separatrix is reduced to the vicinity of the H→L backtransition, the completely detached high-confinement (CDH-) mode is obtained, with small, frequent type-III like ELMs which are almost completely buffered by the divertor plasma before reaching the target plate. This regime would be very attractive for a next step fusion device because it solves the problem of target power overload. The possibility of a CDH-mode in a reactor depends on the magnitude of the L→H and H→L (separatrix) power thresholds as well as on the edge temperature and density which determine the fraction of power radiated inside the separatrix. The extrapolation of these parameters to reactor conditions seems to be quite uncertain at the moment and needs further investigation.

References

[1] LACKNER, K., CHODURA, R., KAUFMANN, M., NEUHAUSER, J., RAUH, K. G., and SCHNEIDER, W., Plasma Phys. Controlled Fusion **26** (1984) 105.

[2] SAMM, U., BERTSCHINGER, G., BOGEN, P., HEY, J. D., HINTZ, E., KÖNEN, L., LIE, Y. T., POSPIESZCZYK, A., SCHORN, R. P., SCHWEER, B., TOKAR, M., and UNTERBERG, B., Plasma Phys. Controlled Fusion **35** (1993) B167.

[3] BECKER, G., 'Transport simulations of ITER with broad density profiles and high radiative fraction', submitted to Nuclear Fusion .

[4] DOYLE, E. J., GROEBNER, R. J., BURRELL, K. H., GOHIL, P., et al., Phys. Fluids B **3** (1991) 2300.

[5] RYTER, F., BÜCHL, K., FUCHS, C., GEHRE, O., GRUBER, O., et al., Plasma Phys. Controlled Fusion **36** (1994) A99.

[6] VON HELLERMANN, M., BREGER, P., FRIELING, J., KÖNIG, R., MANDL, W., MAAS, A., and SUMMERS, H. P., Report JET-P(94)20, to be published in Plasma Physics and Controlled Fusion .

[7] KALLENBACH, A. and MAYER, H. M., Rev. Sci. Instrum. **64** (1993) 1257.

[8] SHARPTON, F. A., JOHN, R., LIN, C., and FAJON, F., Phys. Rev. A **2** (1970) 1305.

[9] HAAS, G., GERNHARDT, J., KEILHACKER, M., MESERVEY, E. B., and THE ASDEX TEAM, J. Nucl. Mater. **121** (1984) 151.

[10] NEU, G., AUBANEL, C., MERTENS, V., RAUPP, G., RICHTER, H., ZASCHE, D., and ZEHETBAUER, T., Proc. 18th Symposium on Fusion Technology (SOFT), in press (1994).

[11] SCHISSEL, D. P., DEBOO, J. C., BURRELL, K. H., FERRON, J. R., GROEBNER, R. J., et al., Nucl. Fusion **31** (1991) 73.

[12] KALLENBACH, A., NEU, R., POSCHENRIEDER, W., and THE ASDEX UPGRADE TEAM, Nuclear Fusion, in press **12** (1994).

[13] GRUBER, O., KALLENBACH, A., KAUFMANN, M., et al., 'Observation of continuous divertor detachment in ASDEX Upgrade', submitted to Physical Review Letters .

[14] YUSHMANOV, P. N., TAKIZUKA, T., RIEDEL, K. S., KARDAUN, O. J. W. F., CORDEY, J. G., KAYE, S. M., and POST, D. E., Nucl. Fusion **30** (1990) 1999.

[15] LAZARUS, E. A., BELL, J. D., BUSH, C. E., et al., Nucl. Fusion **25** (1985) 135.

[16] MESSIAEN, A. M., ONGENA, J., and SAMM, U., E. A., Nucl. Fusion **34** (1994) 825.

[17] SCHISSEL, D. P., Ali MAHDAVI, M., DEBOO, J. C., and LE, M., Nucl. Fusion **34** (1994) 1401.

[18] MONIER-GARBET, P., CHAMOUARD, C., DEMICHELIS, C., et al., Controlled Fusion and Plasma Physics, Proceedings of the 21st Conference, Montpellier (1994) 738.

[19] BEHRINGER, K., 'Description of the impurity transport code STRAHL', JET-R(87)08, JET Joint Undertaking, Culham (1987).

[20] SUMMERS, H. P., 'Atomic data and Analysis Structure', JET-IR 06, JET Joint Undertaking, Culham (1994).

[21] SYNAKOWSKI, E. J., EFTHIMION, P. C., REWOLDT, G., et al., Phys. Fluids B **5** (1993) 2215.

[22] KALLENBACH, A., FUSSMANN, G., MAYER, H.-M., PITCHER, S., and THE ASDEX UPGRADE TEAM, Plasma Phys. Controlled Fusion **36** (1994) 1299.

[23] FUSSMANN, G. FIELD, A. R., KALLENBACH, A., KRIEGER, K., STEUER, K.-H., and THE ASDEX-TEAM, Plasma Phys. Controlled Fusion **33** (1991) 1677.

[24] BESSENRODT-WEBERPALS, M., SÖLDNER, F. X., MÜLLER, E. R., et al., Plasma Phys. Controlled Fusion **34** (1992) 443.